

Behind the scenes of the Quantum Extreme Learning Machines

A. De Lorenzis^{1,2,*}, M. P. Casado^{1,3},

N. Lo Gullo^{4,5}, T. Lux¹, F. Plastina^{4,5} and A. Riera²

¹*Institut de Física d'Altes Energies (IFAE) - The Barcelona Institute of Science and Technology (BIST),
Campus UAB, 08193 Bellaterra (Barcelona), Spain*

²*Qilimanjaro Quantum Tech S.L., Carrer de Venèçuela, 74, 08019 Barcelona, Spain*

³*Departament de Física, Universitat Autònoma de Barcelona*

⁴*Dipartimento di Fisica, Università della Calabria, 87036 Arcavacata di Rende (CS), Italy*

⁵*INFN, gruppo collegato di Cosenza, 87036 Arcavacata di Rende (CS), Italy*

* E-mail: adelorenzis@ifae.es

Abstract

In recent years, Quantum Machine Learning (QML) has grown rapidly, emerging as a promising approach to make quantum computing implementation competitive. In this work, we investigate Quantum Extreme Learning Machines (QELM), a quantum variant of Extreme Learning Machines where training is restricted to the output layer. The proposed architecture combines dimensionality reduction (via PCA or Autoencoders), quantum state encoding, evolution under an XX Hamiltonian, and measurement, providing features for a single-layer classifier.

By analyzing the performance of QELMs as a function of the evolution time, we identify a relatively sharp transition from a low-accuracy to a high-accuracy regime, after which the accuracy saturates. Remarkably, the saturation value matches that achieved with random unitaries, which induce maximally complex dynamics and optimally scramble information across the system. Across all cases studied, the critical transition time is sufficient for information to reach nearest neighbors, enabling feature extraction for learning, and is independent of the system size (i.e., the number of qubits). This independence implies that QELMs can be efficiently simulated classically for a broad class of tasks.

1 Introduction

Over the past two decades, quantum computing has evolved from a theoretical concept into a promising technological frontier, with potential applications that span fields such as chemistry, cryptography, finance, and artificial intelligence [1–4]. Recent advances in hardware and algorithm development [5–8] have significantly accelerated progress, fostering renewed interest in practical quantum-enhanced solutions.

A particularly active area of research is Quantum Machine Learning (QML) [9–13], which seeks to exploit quantum mechanical principles to augment or outperform classical machine learning methods. Exploiting the computational richness of quantum systems, QML aims to tackle problems that are intractable or computationally inefficient for classical methods. [14–20].

Within this framework, we focus on the Quantum Extreme Learning Machine (QELM) [20–30], a quantum adaptation of the classical Extreme Learning Machine (ELM) [31–35]. The ELM paradigm

simplifies learning by confining optimization to the output layer, and this core idea is preserved in QELMs through the use of a static quantum reservoir, a quantum system with fixed internal dynamics. Input data are encoded into quantum states, evolved through the reservoir, and then projected into a high-dimensional feature space, where only the final output weights are trained.

QELMs stand out for their computational efficiency: they do not require the iterative parameter updates typical of conventional deep learning models, leading to faster training and reduced resource demands. Additionally, thanks to the exponential expressivity of quantum Hilbert spaces, QELMs can uncover complex patterns and non-linear relationships within data, making them powerful tools for classification and regression tasks [36, 37].

QELMs fall within the broader framework of Quantum Reservoir Computing (QRC) [29, 38–40], but distinguish themselves for their memoryless nature, where the reservoir’s dynamics reduce to a static, high-dimensional input transformation.

Within the broader QRC framework, explored

across diverse physical platforms such as spin chains [41–50], fermionic and bosonic systems [51–53], and Rydberg atoms [54–58], QELMs emerge as a streamlined and efficient approach.

Throughout this paper, in order to better understand the capabilities of Quantum Extreme Learning Machines, we investigate how their performance depends on the duration of the quantum evolution. We studied the evolution time under a given Hamiltonian and across a wide range of problem settings, we observe a general and robust behavior:

1. Performance exhibits a relatively sudden transition as a function of the evolution time.
2. Beyond the transition point, accuracy saturates, no further improvement is observed with longer evolutions.

With the aim to analyzing this behavior, we organize the paper as follows: Section 2 describes the modelling framework, Sections 3 and 4 deal the performance as a function of evolution time and the accuracy plateau. Instead sections 5 and 6 cover the critical transition time and its implications and finally, section 7 presents our conclusions.

2 Structure and Design of the Adopted Quantum Extreme Learning Machines

In this work, we investigate a Quantum Extreme Learning Machine (QELM) architecture that integrates a classical Extreme Learning Machine (where only the output layer is subject to training) with a quantum reservoir. A schematic overview [26] of the proposed model is provided in Fig.1.

1. *Feature reduction*: One of the main challenges in applying quantum machine learning lies in the limited number of qubits currently available in quantum hardware. Since many real-world datasets exhibit high-dimensional feature spaces, it becomes essential to employ dimensionality reduction techniques that retain as much of the original information as possible while adapting the data to the constraints of the quantum reservoir. To this end, we compress the input data into a compact latent representation before feeding it into the quantum model. This reduction is achieved through two distinct approaches: Principal Component Analysis (PCA) and Autoencoders (AEs) [59–62]. PCA is a linear statistical method that projects the original features onto a set of orthogonal components, ranked by their

variance, thereby preserving the most informative directions in the data. In contrast, Autoencoders are nonlinear neural networks trained to reproduce the input at the output by passing it through a bottleneck structure. The encoding process maps the data into a lower-dimensional latent space, which is then reconstructed by the decoder.

2. *Quantum Encoding of Classical Data*: Before quantum processing can take place, classical data must be encoded into quantum states that can be handled by the quantum system. In our approach, this is done by initializing each qubit in a pure state derived from the input features. A single qubit’s pure state can be visualized as a point on the Bloch sphere:

$$|\psi\rangle = \cos\left(\frac{\theta}{2}\right)|0\rangle + e^{i\phi}\sin\left(\frac{\theta}{2}\right)|1\rangle \quad (1)$$

where $\theta \in [0, \pi]$ and $\phi \in [0, 2\pi]$. This geometric representation enables the encoding of real-valued data by mapping feature values to these two angles.

We adopt a dense angle encoding strategy, where each qubit is initialized using two classical features: one mapped to the polar angle θ and the other to the azimuthal angle ϕ . The complete initial quantum state of the system, composed of $N = \lceil M/2 \rceil$ qubits for a feature vector $\vec{x} = [x_1, \dots, x_M]^T \in \mathbb{R}^M$ is given by:

$$|\vec{x}\rangle = \bigotimes_{i=1}^{\lceil M/2 \rceil} \left(\cos\left(\frac{x_{2i-1}}{2}\right)|0\rangle + e^{ix_{2i}}\sin\left(\frac{x_{2i-1}}{2}\right)|1\rangle \right) \quad (2)$$

Here, each pair of features (x_{2i-1}, x_{2i}) is used to set the state of the i -th qubit, effectively allowing each qubit to encode two features. All input features are normalized to the interval $[0, \pi]$ to ensure valid quantum states. This encoding efficiently maps high-dimensional classical inputs into a quantum state suitable for further processing, while respecting the qubit limitations of current hardware.

3. *Quantum layer and time evolution*: Once the classical data has been encoded into a quantum state, the system undergoes time evolution governed by a Hamiltonian operator. This evolution, carried out within the quantum layer, transforms the initial state through unitary dynamics. In our implementation, the system evolves under the action of the following Hamiltonian XX model with interaction

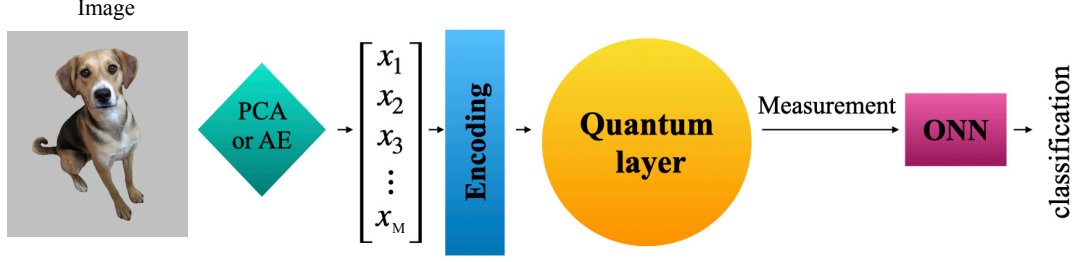


Figure 1: Schematic representation of the QELM architecture. The workflow consists of the following steps: dimensionality reduction using either PCA or an Autoencoder (AE); encoding of the classical data into an initial quantum state; time evolution through the quantum layer; measurement of the evolved quantum state; and final classification via a classical single-layer neural network. Image for illustrative purposes only.

between nearest neighbours, assuming periodic boundary conditions:

$$H = \frac{1}{2} \sum_{i=1}^N (\sigma_x^{(i)} \sigma_x^{(i+1)} + \sigma_y^{(i)} \sigma_y^{(i+1)}). \quad (3)$$

4. *Measurement and Classification:* After the quantum evolution governed by the selected Hamiltonian, the final state is measured in the computational basis. This process yields classical information corresponding to the probability distribution over basis states, i.e., the population of the wave function.

In a real quantum experiment, such information is typically obtained by repeatedly measuring identically prepared quantum states, due to the probabilistic nature of quantum measurements. In our work, we simulate this process and extract a classical feature vector of 2^N real values per input, where N is the number of qubits. These features are then fed into a classical simple One-layer Neural Network (ONN) with softmax activation, which performs the final classification. The architecture of the classifier is defined by the number of quantum measurement outputs and the number of target classes, and is trained using the Adam optimizer with categorical cross-entropy loss. For the numerical implementation, we used the Keras framework.

2.1 Datasets

In this section, we describe the benchmark datasets used to train and evaluate our QELM model: MNIST [63], Fashion-MNIST [64] and CIFAR-10 [65]. Figure 2 provides a visual overview of these datasets, with one representative image per class.

- **MNIST:** The MNIST (Modified National Institute of Standards and Technology)

dataset is a classical benchmark for handwritten digit classification. It contains 70,000 grayscale images of 28×28 pixels, split into 60,000 training and 10,000 test samples. Each image represents a digit from 0 to 9.

- **Fashion-MNIST:** Fashion-MNIST is a drop-in replacement for MNIST, designed to provide a more challenging classification task. It consists of 70,000 grayscale images of clothing items, also sized 28×28 pixels, divided into 10 categories such as shirts, shoes, and coats. Like MNIST, it provides 60,000 training and 10,000 test images.
- **CIFAR-10:** CIFAR-10 is a dataset of 60,000 color images (RGB) at 32×32 pixel resolution, distributed equally among 10 classes, including objects such as airplanes, cats, and trucks. It is split into 50,000 training and 10,000 test images. Due to the diversity and visual complexity of the images, CIFAR-10 serves as a standard benchmark for evaluating image classification algorithms in more realistic settings.

3 Performance as a Function of Evolution Time

After reducing the dataset images to $2N$ features and encoding them using dense angle encoding, we evolved the system and conducted the measurements. These coefficients were then fed into a single-layer neural network, which provided us with the resulting classification accuracies.

We performed the classification and calculated the accuracies for different evolution times and studied the performance in terms of achieved accuracy as a function of evolution time.

In Fig. 3, 4 and 5 we can see these plots respectively for the MNIST, Fashion-MNIST and CIFAR-

10 datasets, with the training results shown on the left and the test results on the right. The colors of the curves represent the different number of qubits employed in the algorithm. For the simpler datasets, such as MNIST and Fashion-MNIST, we employed between 6 and 10 qubits, whereas for the more complex dataset CIFAR-10, results were plotted for 6 to 11 qubits. Simulating quantum computers with many qubits requires substantial computational resources, so our study was limited to systems of manageable size.

The figures show that each curve remains nearly constant at first. After a certain time interval, the accuracy increases sharply and eventually converges to a plateau. There is thus a relatively narrow transitional time window during which the performance rises until it stabilizes. We observe that, regardless of the system size or the dataset used, the performance reaches a steady state at time t_* , which occurs around 1.

The curves are shifted upward as N increases, which is expected since the number of features used in the algorithm grows with N , specifically as $2N$.

In sum, we observe that there is a transition time t_* at which the accuracy exhibits a sudden jump, and a saturation accuracy A_* that the system reaches after the transition time t_* .

In the following sections, we aim to explain the reason behind these values of saturation accuracy A_* and transition time t_* .

4 Information Propagation and the Accuracy Plateau

Recently, Ref. [20] proposed a connection between the performance of QELM and the phenomenon of information scrambling. In quantum information, scrambling refers to the irreversible spreading of information throughout a system. Broadly speaking, scrambling is detrimental to processes such as QELM, where the input and output of the computation must remain correlated. If the information becomes fully scrambled, the input is effectively lost, and no link to the output remains. However, the impact of scrambling depends strongly on the observables under consideration. When focusing on local quantities, such as magnetization or correlation functions, scrambling is related to the thermalization of subsystems, which erases correlations between the encoded input data and the measured outcomes. As the size of the subsystem increases, the effect of scrambling diminishes. In the limit where the subsystem approaches the size of the entire system, it becomes possible to recover a mapping between the input and the output by measuring global observables. In our framework, these

global observables correspond to the probabilities of finding the system in specific bit-string states (computational basis states). The recovery of the input–output mapping, despite local scrambling, arises because the dynamics of global observables remain unitary. Thus, although a Hamiltonian that induces system-wide information spreading leads to information loss when viewed locally, it can actually enhance input distinguishability when measured globally. To test this idea, we consider random unitary matrices, which can serve as models of system dynamics. Such random unitaries are, in fact, well-suited to maximize the spreading of information from the initial state across the entire system.

In Figs. 3, 4, and 5 (horizontal dashed lines), we show the performances of the QELM using a random unitary matrix. Since different random unitaries can lead to different accuracies, the dashed lines correspond to the average over 10 independent samples (taken from the Haar measure). The associated standard deviation is indicated by the shaded area. The different system sizes are represented by different colours, consistent with the colour code used for the Hamiltonian evolution.

We find that the saturation performance A_* obtained for every system size coincides with the performance achieved by a random unitary, in agreement with the intuition that classification benefits from information spreading.

This observation is particularly remarkable, given that the XX Hamiltonian employed in the QELM is:

- Highly specific and the evolution operator it generates is far from random,
- Translational invariant,
- Integrable, as it can be diagonalized through a Jordan–Wigner transformation followed by a Fourier transform.

The explanation lies in the structure of the encoding scheme. In this setup, the initial state significantly overlaps with nearly all many-body eigenstates of the XX model. As a result, the dynamics is not confined to integrable sectors but effectively explores the entire Hilbert space.

5 Critical Transition Time and Locality

Once we have understood the saturation value A_* of the accuracy, let us now address the question of the transition time t_* .

A natural first guess, consistent with the intuition of information spreading across the system,

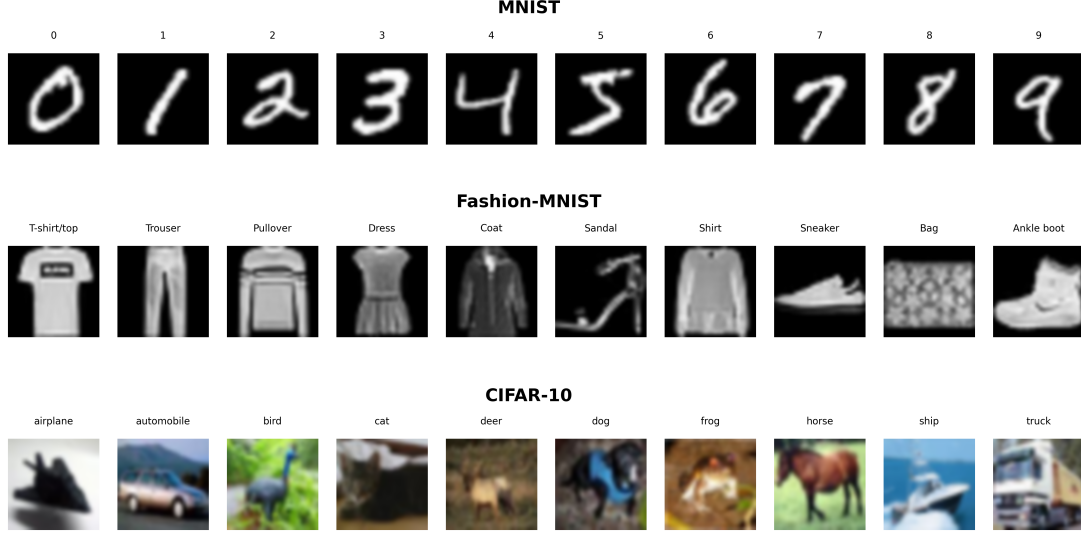


Figure 2: Sample images from three widely used benchmark datasets in this study. The top row displays handwritten digits from MNIST (digits 0–9), the middle row shows clothing items from Fashion-MNIST (10 clothing categories), and the bottom row presents natural object categories from CIFAR-10. Each column corresponds to one class, labeled above each image.

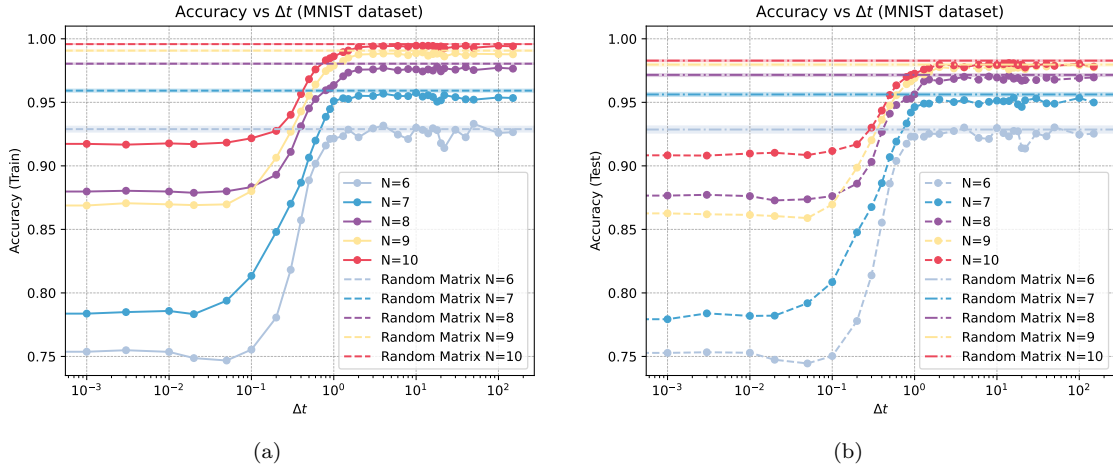


Figure 3: Training (left panel) and testing (right panel) accuracy as a function of evolution time using the MNIST dataset. The time evolution and the encoding have been performed with the Hamiltonian XX model and the dense angle, respectively. The horizontal dashed lines indicate the performance obtained using a random unitary matrix, specifically by performing 10 measurements and computing the mean and standard deviation.

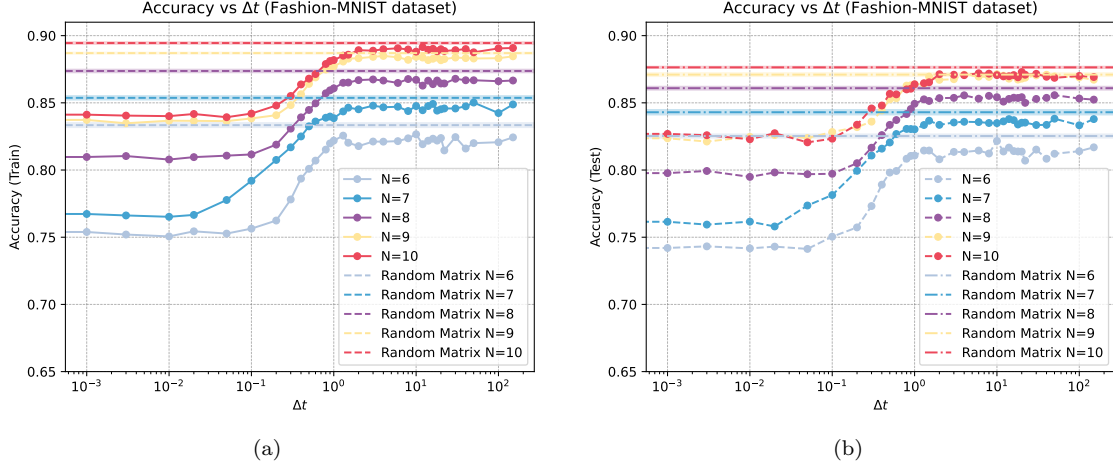


Figure 4: Training (left panel) and testing (right panel) accuracy as a function of evolution time using the Fashion-MNIST dataset. The time evolution and the encoding have been performed with the Hamiltonian XX model and the dense angle, respectively. The horizontal dashed lines indicate the performance obtained using a random unitary matrix, specifically by performing 10 measurements and computing the mean and standard deviation.

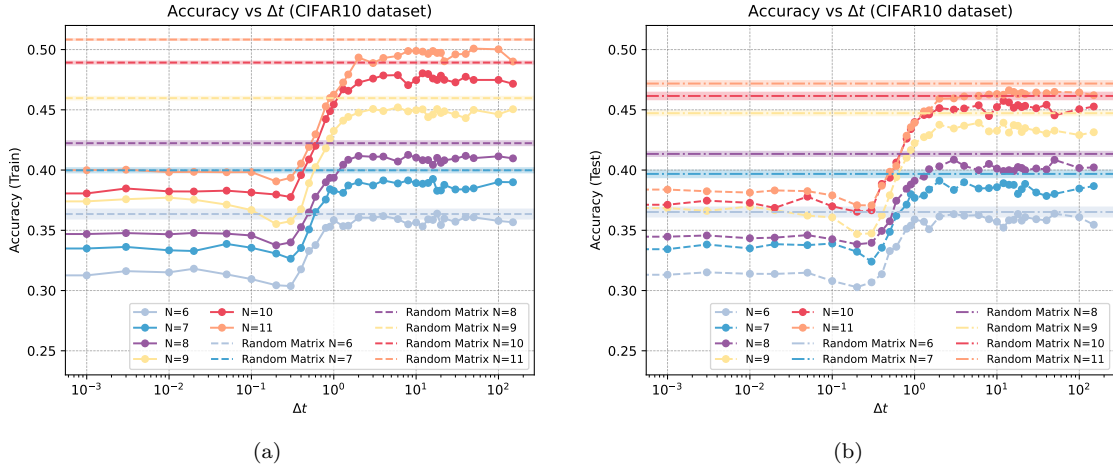


Figure 5: Training (left panel) and testing (right panel) accuracy as a function of evolution time using the CIFAR-10 dataset. The time evolution and the encoding have been performed with the Hamiltonian XX model and the dense angle, respectively. The horizontal dashed lines indicate the performance obtained using a random unitary matrix, specifically by performing 10 measurements and computing the mean and standard deviation.

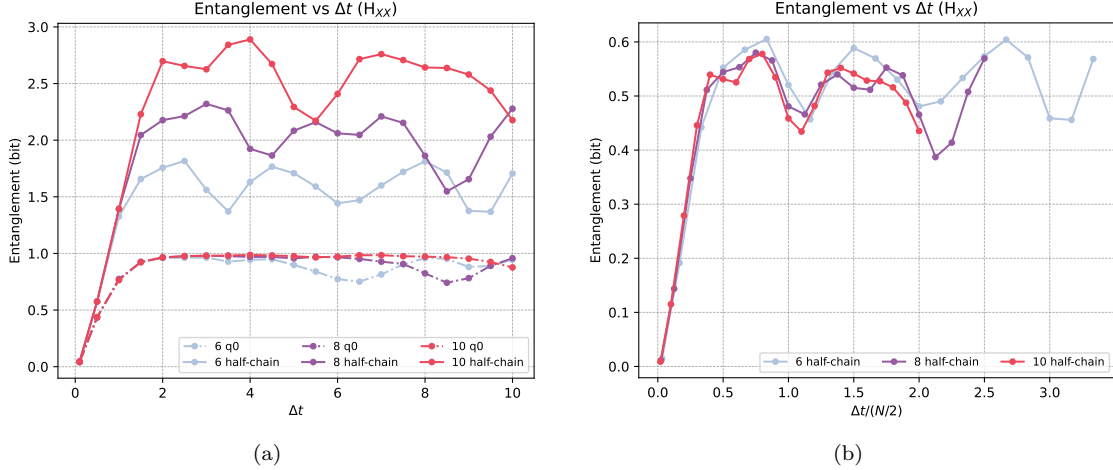


Figure 6: a) Von Neumann entropy as function of the evolution time of half-chain (solid lines) and of the single qubit (dash-dotted lines). The colors denote the different sizes N ($N=6, 8, 10$) of the entire system. b) Normalized (with $N/2$) von Neumann entropy as function of the evolution time (divided by $N/2$) of half-chain.

is that the transition time corresponds to the characteristic timescale required for initially localized information on individual qubits to spread throughout the system.

To substantiate this intuition, it is useful to introduce the notion of an effective speed of information propagation. Although in non-relativistic quantum mechanics space and time are treated on different footings, and supra-luminal influences of the wave function are, in principle, possible, the Lieb–Robinson bounds demonstrate that for local Hamiltonians—such as our XX model—there exists an effective causal structure. In practice, this establishes a maximum velocity at which quantum dynamics can propagate information.

In Appendix A we determine the Lieb–Robinson velocity for the XX model defined in Eq. (3) and show that it is equal to 1. Combining this result with the plots presented in the previous section, two conclusions follow:

- From a qualitative perspective, the absence of a linear dependence between the transition time and the system size rules out the hypothesis that the information must spread across the entire system.
- Quantitatively, up to the transition time t_* , the information remains confined to the qubit of origin and its nearest neighbors.

To better visualize how information spreads across the system and to confirm the above insights, in Fig. 6(a) we plot the von Neumann entropy of half the chain together with the single-qubit von Neumann entropy as functions of the evolution time.

These quantities provide complementary perspectives: the half-chain entropy captures the buildup of bipartite entanglement across the system, while the single-qubit entropy reflects the local delocalization of information.

The evolution of the single-qubit entropy shows that the quantum information initially encoded in one qubit becomes entangled with its environment after an evolution time of order 1, irrespective of the total system size. In contrast, the entanglement entropy of half the chain grows linearly with time until it saturates. The growth rate is identical for all system sizes, indicating that the speed of information propagation is independent of system size, while the saturation value scales proportionally to the block size ($N/2$). These results on the entanglement dynamics of spin chains are well established in the literature [66, 67] and are explained by the ballistic propagation of quasiparticle excitations, which travel in opposite directions in entangled pairs.

It is also interesting to note that the curves of half-chain entropy presented in Fig. 6(a) obey a scaling law of the form

$$S_N(t) = N f\left(\frac{t}{N}\right), \quad (4)$$

where $S_N(t)$ denotes the half-chain entropy for a system of N sites at time t . One could expect this relation to hold for large N ; but, in fact, it approximately holds even for not so large N 's. Indeed, the scaling function f is shown in Fig. 6(b), where the normalized entropy $S_N/(N/2)$ is plotted as a function of t/N for the system sizes $N = 6, 8$, and 10 .

Several features of f are worth highlighting:

- The entropy grows linearly until it saturates at $t = N/2$.
- For $t > N/2$, the entropy exhibits oscillations with characteristic periodicities $T \simeq 0.5$ and $T \simeq 1$.

These properties of the scaling function f confirm the intuition of ballistic information propagation. The linear growth for $t < N/2$ arises from pairs of entangled quasiparticles located on opposite sides of the bipartition: the longer the time, the more quasiparticles cross its boundary and contribute to the entropy. Once the block is filled with quasiparticles, the entropy saturates, since quasiparticles are simultaneously entering and leaving. The oscillations observed for $t > N/2$ are a consequence of all quasiparticles propagating with similar velocities but carrying different amounts of entanglement.

The confirmation of the ballistic information propagation model, together with the observation of a transition time t_* at which the information has only spread across a local region of a few neighbors, suggests that our naive real-space picture of information spreading is not the key feature for explaining the information processing capacity of the QELM. This indicates that the analysis should instead be carried out in a different space.

6 Implications for Classical Simulability

In the previous section, we have seen that contrary to initial expectations, it appears that information from a single site does not need to spread across the entire system to achieve optimal accuracy. Instead, spread of information to the nearest neighbors seems to be enough to extract the relevant features needed for learning.

The apparent observation that the maximum accuracy can be reached for a time which is independent of the system size has a profound implication for the classical simulability of QELM. More specifically, it suggests that shallow quantum circuits may be sufficient to achieve the same performance as QELM. However, shallow circuits with limited entanglement can be efficiently simulated using classical methods, such as matrix product states (MPS). This challenges the claim of quantum advantage, as the learning process may not require computational resources beyond those accessible classically.

In order to confirm the previous hypothesis, we realized a new implementation (see Fig. 7). Using the same reduced features employed as input for the QELM, and consistently applying dense angle encoding (thereby maintaining the same initial state) we applied then blocks of a unitary random

G for pairs of qubits contiguous. At each layer the unitary matrix is translated by one qubit. The algorithm ensures that at each layer the information carried in the qubits is mixed only locally. As the depth increases, information is shared across ever larger qubits.

We applied the new algorithm to the MNIST and CIFAR-10 datasets and evaluated the accuracy as a function of the number of layers. The results are shown in Fig. 8 and Fig. 9. For the MNIST dataset, we observe that four layers are sufficient to reach the accuracy plateau, independently of the system size. A similar behavior is found for CIFAR-10 at small system sizes; however, for larger N the accuracy saturates only after the fifth or sixth layer. This slight dependence of the required number of layers on the system size in the CIFAR-10 case suggests that the classical simulability of QELMs may be problem-dependent.

7 Conclusions and Outlook

In this work, we investigated several aspects of the Quantum Extreme Learning Machines for the classification tasks, beginning with an analysis of their performance as a function of evolution time and subsequently examining their behavior in greater detail.

So initially we reduced the dataset images (with PCA or AE) in vectors of $2N$ features, we encoded them using the Dense Angle encoding in the quantum layer, then we performed the temporal evolution of the quantum state under the Hamiltonian H_{XX} . After the evolution we measured the output state in the computational basis, so we obtained 2^N real values for each image which were then fed to the machine learning classifier.

Graphing the performance as function of the time evolution we observed that the accuracy exhibits a relatively sudden transition and beyond the transition point, the performance saturates.

Furthermore when analyzing the plateau value, we find that the performance is close to that achieved using random unitaries, where the dynamics are maximally complex and are well-suited to maximize the spreading of information from the initial state across the entire system.

About this aspect, we deduce that even simple Hamiltonians can generate dynamics that are sufficiently complex to spread information effectively, distributing it through the Hilbert space and enabling good performance on learning tasks. Studying instead, the critical transition time, we understand that it is sufficient for information to be shared with nearest neighbors to extract the relevant features needed for learning.

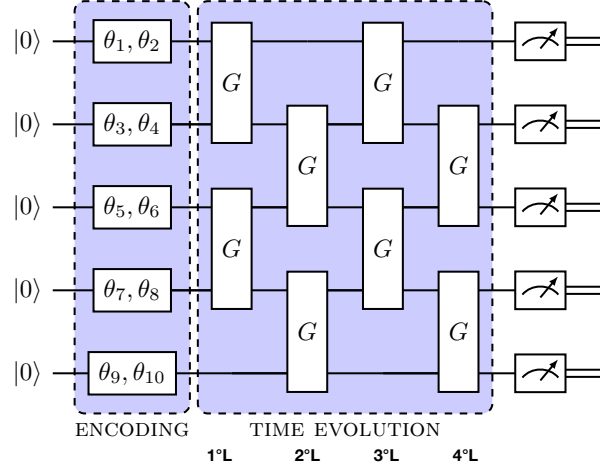


Figure 7: A schematic representation of an algorithm with 5 qubits, in which a unitary random matrix is applied for pairs of qubits contiguous.

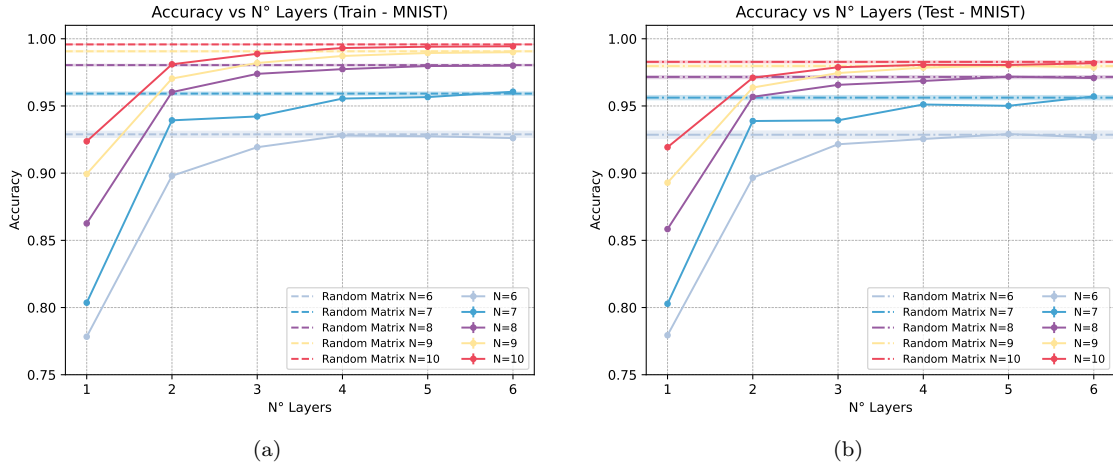


Figure 8: Training (left panel) and testing (right panel) accuracy as a function of the number of layers using the MNIST dataset.

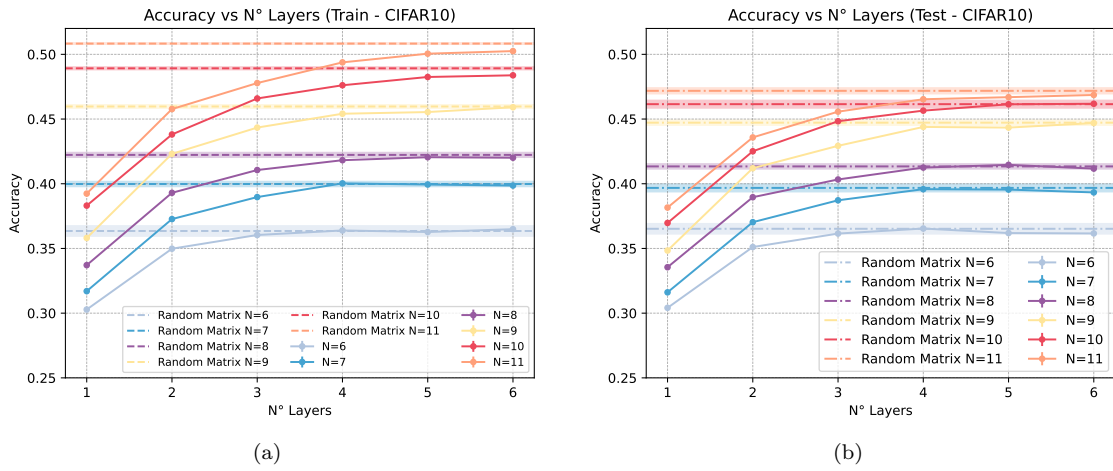


Figure 9: Training (left panel) and testing (right panel) accuracy as a function of the number of layers using the CIFAR-10 dataset.

This locality suggests that QELMs may be classically simulable for a wide family of tasks, as their performance does not rely on highly non-local or deeply entangled dynamics.

Acknowledgments

The research leading to these results has received funding from the Spanish Ministry of Science and Innovation PID2022-136297NB-I00/AEI/10.13039/501100011033/ FEDER, UE. IFAE is partially funded by the CERCA program of the Generalitat de Catalunya. The results have received funds from the program Plan de Doctorados Industriales of the Research and Universities Department of the Catalan Government (2022 DI 011). This work was partially funded by the Generalitat de Catalunya, AGAUR 2021-SGR-01506 and partially supported by the PNRR MUR Project No. PE0000023-NQSTI through the secondary projects QuCADD and ThAnQ. We acknowledge the use of the Finnish CSC facilities under the project 2010295 "Quantum Reservoir Computing". We gratefully acknowledge the use of RES resources provided by the Barcelona Supercomputing Center through project FI-2025-1-0043 on MareNostrum 5.

A Appendix: Lieb-Robinson Bounds: General Statement

Consider a quantum spin system defined on a lattice Λ , with local Hilbert space \mathcal{H}_i at each site $i \in \Lambda$, and a Hamiltonian of the form:

$$H = \sum_{X \subset \Lambda} \Phi(X), \quad (5)$$

where $\Phi(X)$ are local interaction terms supported on finite subsets $X \subset \Lambda$.

We assume that:

- The local interaction terms $\Phi(X)$ are uniformly bounded: $\|\Phi(X)\| \leq J$ for some constant $J > 0$.
- The interactions are of finite range r_0 or decay exponentially with distance.

Under these assumptions, the Lieb-Robinson bound asserts that for any two observables A and B supported on disjoint regions $X, Y \subset \Lambda$, the following holds:

$$\|A(t), B\| \leq c \|A\| \|B\| e^{-\mu(d(X,Y) - v|t|)}, \quad (6)$$

where c , μ and v are positive constants. The Lieb-Robinson velocity v depends linearly on the

bound J of the interaction terms and scales as $v \propto J$.

This captures the idea that stronger local interactions permit faster information propagation across the system.

A.1 Application to the XX Model

The one-dimensional XX model describes nearest-neighbor spin interactions:

$$H = J \sum_{j=1}^{N-1} (\sigma_j^x \sigma_{j+1}^x + \sigma_j^y \sigma_{j+1}^y) = \sum_{j=1}^{N-1} (\sigma_j^+ \sigma_{j+1}^- + \sigma_j^- \sigma_{j+1}^+) \quad (7)$$

where $\sigma_j^\pm = (\sigma_j^x \pm i\sigma_j^y)/2$.

Using the Jordan-Wigner transformation, this model maps to free fermions:

$$H = \sum_{j=1}^{N-1} (c_j^\dagger c_{j+1} + c_{j+1}^\dagger c_j) \quad (8)$$

Since the Hamiltonian is quadratic, the Heisenberg evolution $c_j(t)$ remains linear:

$$c_j(t) = \sum_k u_{jk}(t) c_k, \quad u_{jk}(t) = i^{j-k} J_{j-k}(2Jt), \quad (9)$$

where J_n is the Bessel function of the first kind. Therefore, the commutator between distant fermionic operator is:

$$\|[c_j(t), c_k^\dagger]\| = u_{jk}(t) = |J_{j-k}(2Jt)| \leq C e^{-\mu(|j-k| - 2Jt)}, \quad (10)$$

which explicitly realizes the Lieb-Robinson bound with velocity:

$$v_{LR} = 2J. \quad (11)$$

A.2 Group Velocity and its Connection to Lieb-Robinson Bounds

The free-fermion Hamiltonian can be diagonalized with Fourier modes:

$$c_j = 1/\sqrt{N} \sum_k e^{ikj} a_k, \quad (12)$$

with $k = 2\pi m/N$ with $m \in \mathbb{Z}_N$. The Hamiltonian becomes:

$$H = \sum_k \epsilon(k) a_k^\dagger a_k, \quad \epsilon(k) = 2J \cos(k). \quad (13)$$

where $\epsilon(k)$ is the dispersion relation.

The group velocity is then given by:

$$v_g(k) = \frac{d\epsilon(k)}{dk} = -2J \sin(k). \quad (14)$$

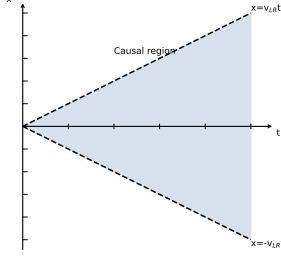


Figure 10: Lieb-Robinson light cone with velocity $v_{LR} = 2J$. Outside this region, commutators of local observables are exponentially suppressed.

Its maximum over $k \in [-\pi, \pi]$ reads

$$v_{max} = \max_k |v_g(k)| = 2J = v_{LR}. \quad (15)$$

Thus, the Lieb-Robinson velocity coincides with the maximal group velocity of the system's excitations.

A.3 Information Propagation from a Localized Excitation

Consider a localized excitation created at $t=0$:

$$|\psi(0)\rangle = c_j^\dagger |0\rangle. \quad (16)$$

Its time evolution:

$$|\psi(t)\rangle = c_j^\dagger(t) |0\rangle, \quad c_j^\dagger(t) |0\rangle = \sum_k i^{k-j} J_{k-j}(2Jt) c_k^\dagger, \quad (17)$$

shows that the amplitude on site k is $|J_{k-j}(2Jt)|$, which is peaked around $|k - j| \approx 2Jt$, and decays exponentially outside.

This illustrates a ballistic propagation of the excitation with a velocity $v = 2J$ and confirms that information spreads within a light cone determined by the Lieb-Robinson bound (see Fig.10).

A.4 Accuracy saturation, Lieb-Robinson velocity and quantum advantage

In Figures 3, 4 and 5 we show how the accuracy of a QELM depends on the total quantum evolution time for different system sizes and problems. As expected, the accuracy increases with time until it saturates at a value that depends on the size of the quantum reservoir: larger systems achieve higher saturation accuracy.

Two complementary observations can be drawn from this plot.

First, from a qualitative perspective, the saturation time, the point at which the accuracy plateaus, appears to be largely independent of the system size. Second, from a quantitative standpoint, we can relate this behavior to how far information spreads within the system. Notably, all system sizes

reach their maximum accuracy at approximately time $t=1$. According to the Lieb-Robinson bound derived in the previous section, this corresponds to quantum information propagating over a distance of about one lattice site,

$$d = v_{LR} \cdot t = (2J)t = 2 \cdot \frac{1}{2} \cdot 1 = 1. \quad (18)$$

B Appendix: The choice of Measurement Basis

In addition to allowing the QELM sufficient time to evolve, it is also crucial to consider the choice of the measurement basis. In particular, the measurement basis should be sufficiently distinct from the eigenbasis of the Hamiltonian governing the evolution. This distinction plays a significant role in the expressiveness and information content of the output features extracted via measurement.

B.1 Quantum Evolution and Basis Representations

Assume the quantum system underlying the QELM evolves under a time-independent Hamiltonian H , with spectral decomposition:

$$H = \sum_k E_k |E_k\rangle \langle E_k|, \quad (19)$$

where $|E_k\rangle$ are the eigenstates and E_k the corresponding eigenvalues.

The features of each input data sample are encoded into an initial quantum state $|\psi(0)\rangle$, which can be expanded in the Hamiltonian eigenbasis as:

$$|\psi(0)\rangle = \sum_n c_n |E_n\rangle. \quad (20)$$

After an evolution time t , the system evolves into:

$$|\psi(t)\rangle = \sum_n c_n e^{-iE_n t} |E_n\rangle. \quad (21)$$

Let the measurement be performed in a basis $|s_k\rangle$, which may or may not coincide with the eigenbasis of H . The probability of measuring the system in state $|s_k\rangle$ at time t is given by:

$$p_k(t) = |\langle s_k | \psi(t) \rangle|^2 = \sum_{n,m} \langle s_k | E_n \rangle \langle s_k | E_m \rangle^* e^{-i(E_n - E_m)t} c_n c_m^*. \quad (22)$$

B.2 Relevance of Basis Misalignment

This expression illustrates that the time-dependent measurement statistics $p_k(t)$ are sensitive to the

overlap between the Hamiltonian eigenstates and the measurement basis vectors. If the two bases coincide, time evolution does not generate any non-trivial interference terms, and the dynamics may lack the richness needed for expressive feature extraction. The following scenarios clarify this relationship.

B.3 Identical Hamiltonian and Measurement Bases

If the measurement basis $|s_k\rangle$ coincides with the Hamiltonian eigenbasis $|E_k\rangle$, then all cross terms $n \neq m$ in $p_k(t)$ vanish due to the orthogonality. Consequently, the probabilities $p_k(t)$ become time-independent:

$$p_k(t) = |c_k|^2 (\text{constant in time}). \quad (23)$$

In this case, no interference occurs, and the feature map is static, rendering the QELM ineffective in capturing temporal dynamics.

B.3.1 Mutually Unbiased Bases

When the Hamiltonian and measurement bases are mutually unbiased, that is,

$$|\langle s_k | E_n \rangle|^2 = \frac{1}{d} \forall n, k \Leftrightarrow \langle s_k | E_n \rangle, \quad (24)$$

where d is the dimension of the Hilbert space. In this scenario, the probability amplitudes are evenly distributed, and the evolution induces maximal interference among eigenstate components. As a result, the measurement probabilities $p_k(t)$ exhibit rich time-dependent patterns, enhancing the nonlinear feature encoding capabilities of the QELM.

References

- [1] R. P. Feynman, "Simulating physics with computers," *International journal of theoretical physics*, vol. 21, no. 6/7, pp. 467–488, 1982.
- [2] A. Montanaro, "Quantum algorithms: an overview," *npj Quantum Information*, vol. 2, Jan. 2016.
- [3] M. A. Nielsen and I. L. Chuang, *Quantum Computation and Quantum Information: 10th Anniversary Edition*. Cambridge University Press, 2010.
- [4] P. W. Shor, "Polynomial-time algorithms for prime factorization and discrete logarithms on a quantum computer," *SIAM Journal on Computing*, vol. 26, no. 5, pp. 1484–1509, 1997.
- [5] F. Arute, K. Arya, R. Babbush, D. Bacon, J. Bardin, R. Barends, R. Biswas, S. Boixo, F. Brandao, D. Buell, B. Burkett, Y. Chen, J. Chen, B. Chiaro, R. Collins, W. Courtney, A. Dunsworth, E. Farhi, B. Foxen, A. Fowler, C. M. Gidney, M. Giustina, R. Graff, K. Guerin, S. Habegger, M. Harrigan, M. Hartmann, A. Ho, M. R. Hoffmann, T. Huang, T. Humble, S. Isakov, E. Jeffrey, Z. Jiang, D. Kafri, K. Kechedzhi, J. Kelly, P. Klimov, S. Knysh, A. Korotkov, F. Kostitsa, D. Landhuis, M. Lindmark, E. Lucero, D. Lyakh, S. Mandrà, J. R. McClean, M. McEwen, A. Megrant, X. Mi, K. Michielsen, M. Mohseni, J. Mutus, O. Naeem, M. Neeley, C. Neill, M. Y. Niu, E. Ostby, A. Petukhov, J. Platt, C. Quintana, E. G. Rieffel, P. Roushan, N. Rubin, D. Sank, K. J. Satzinger, V. Smelyanskiy, K. J. Sung, M. Trevithick, A. Vainsencher, B. Villalonga, T. White, Z. J. Yao, P. Yeh, A. Zalcman, H. Neven, and J. Martinis, "Quantum supremacy using a programmable superconducting processor," *Nature*, vol. 574, p. 505–510, 2019.
- [6] H.-S. Zhong *et al.*, "Quantum computational advantage using photons," *Science*, vol. 370, no. 6523, pp. 1460–1463, 2020.
- [7] H.-Y. Huang *et al.*, "Quantum advantage in learning from experiments," *Science*, vol. 376, no. 6598, p. abn7293, 2022.
- [8] J. Preskill, "Quantum Computing in the NISQ era and beyond," *Quantum*, vol. 2, p. 79, 2018.
- [9] J. Biamonte, P. Wittek, N. Pancotti, P. Rebentrost, N. Wiebe, and S. Lloyd, "Quantum machine learning," *Nature*, vol. 549, no. 7671, pp. 195–202, 2017.
- [10] M. Schuld and F. Petruccione, *Machine Learning with Quantum Computers*. Springer, 01 2021.
- [11] M. Schuld and F. Petruccione, *Supervised Learning with Quantum Computers*. Quantum Science and Technology, Springer, 2018.
- [12] I. Cong, S. Choi, and M. Lukin, "Quantum convolutional neural networks," *Nature Physics*, vol. 15, pp. 1–6, 12 2019.
- [13] Z. Liu, P.-X. Shen, W. Li, L. M. Duan, and D.-L. Deng, "Quantum capsule networks," *Quantum Sci. Technol.*, vol. 8, no. 1, p. 015016, 2023.

- [14] M. Schuld, I. Sinayskiy, and F. Petruccione, “The quest for a quantum neural network,” *Quantum Information Processing*, vol. 13, no. 08, p. 2014.
- [15] V. Havlicek, A. D. Córcoles, K. Temme, A. W. Harrow, A. Kandala, J. M. Chow, and J. M. Gambetta, “Supervised learning with quantum-enhanced feature spaces,” *Nature*, vol. 567, pp. 209–212, 2019.
- [16] S. Lloyd, M. Mohseni, and P. Rebentrost, “Quantum algorithms for supervised and unsupervised machine learning,” 7 2013.
- [17] C. Mastroianni, F. Plastina, L. Scarcello, J. Settimo, and A. Vinci, “Assessing quantum computing performance for energy optimization in a prosumer community,” *IEEE Transactions on Smart Grid*, vol. 15, no. 1, pp. 444–456, 2023.
- [18] C. Mastroianni, F. Plastina, J. Settimo, and A. Vinci, “Variational quantum algorithms for the allocation of resources in a cloud/edge architecture,” *IEEE Transactions on Quantum Engineering*, vol. 5, pp. 1–18, 2024.
- [19] M. Consiglio, J. Settimo, A. Giordano, C. Mastroianni, F. Plastina, S. Lorenzo, S. Maniscalco, J. Goold, and T. J. Apollaro, “Variational gibbs state preparation on noisy intermediate-scale quantum devices,” *Physical Review A*, vol. 110, no. 1, p. 012445, 2024.
- [20] M. Vetrano, G. Lo Monaco, L. Innocenti, S. Lorenzo, and G. M. Palma, “State estimation with quantum extreme learning machines beyond the scrambling time,” 9 2024.
- [21] P. Mújal, R. Martínez-Peña, J. Nokkala, J. García-Bení, G. Giorgi, M. Soriano, and R. Zambrini, “Opportunities in quantum reservoir computing and extreme learning machines,” *Advanced Quantum Technologies*, vol. 4, no. 06, p. 2021.
- [22] L. Innocenti, S. Lorenzo, I. Palmisano, A. Ferraro, M. Paternostro, and G. M. Palma, “Potential and limitations of quantum extreme learning machines,” *Communications Physics*, vol. 6, p. 118, May 2023.
- [23] W. Xiong, G. Facelli, M. Sahebi, O. Agnel, T. Chotibut, S. Thanasilp, and Z. Holmes, “On fundamental aspects of quantum extreme learning machines,” 12 2023.
- [24] A. Sakurai, M. P. Estarellas, W. J. Munro, and K. Nemoto, “Quantum Extreme Reservoir Computation Utilizing Scale-Free Networks,” *Phys. Rev. Applied*, vol. 17, no. 6, p. 064044, 2022.
- [25] A. Hayashi, A. Sakurai, W. J. Munro, and K. Nemoto, “Effective quantum feature maps in quantum extreme reservoir computation from the XY model,” *Phys. Rev. A*, vol. 111, no. 2, p. 022431, 2025.
- [26] A. De Lorenzis, M. P. Casado, M. P. Estarellas, N. L. Gullo, T. Lux, F. Plastina, A. Riera, and J. Settimo, “Harnessing quantum extreme learning machines for image classification,” *Phys. Rev. Applied*, vol. 23, no. 4, p. 044024, 2025.
- [27] A. Suprano, D. Zia, L. Innocenti, S. Lorenzo, V. Cimini, T. Giordani, I. Palmisano, E. Polino, N. Spagnolo, F. Sciarrino, G. M. Palma, A. Ferraro, and M. Paternostro, “Experimental property reconstruction in a photonic quantum extreme learning machine,” *Phys. Rev. Lett.*, vol. 132, p. 160802, Apr 2024.
- [28] M. Kornjača *et al.*, “Large-scale quantum reservoir learning with an analog quantum computer,” 7 2024.
- [29] J. Chen, H. I. Nurdin, and N. Yamamoto, “Temporal information processing on noisy quantum computers,” *Phys. Rev. Appl.*, vol. 14, p. 024065, Aug 2020.
- [30] P. D. Solanki and A. Pham, “Harnessing Quantum Dynamics for Robust and Scalable Quantum Extreme Learning Machines,” 3 2025.
- [31] G.-B. Huang, Q.-Y. Zhu, and C.-K. Siew, “Extreme learning machine: a new learning scheme of feedforward neural networks,” in *2004 IEEE International Joint Conference on Neural Networks (IEEE Cat. No.04CH37541)*, vol. 2, pp. 985–990 vol.2, 2004.
- [32] G. Huang, G.-B. Huang, S. Song, and K. You, “Trends in extreme learning machines: A review,” *Neural Networks*, vol. 61, pp. 32–48, 2015.
- [33] S. Ding, H. Zhao, Y. Zhang, X. Xu, and R. Nie, “Extreme learning machine: algorithm, theory and applications,” *Artif. Intell. Rev.*, vol. 44, p. 103–115, June 2015.
- [34] J. Wang, S. Lu, S.-H. Wang, and Y.-D. Zhang, “A review on extreme learning machine,” *Multimedia Tools and Applications*, vol. 81, no. 29, pp. 41611–41660, 2022.

- [35] G.-B. Huang, D. Wang, and Y. Lan, “Extreme learning machines: a survey. int j mach learn cybern,” *International Journal of Machine Learning and Cybernetics*, vol. 2, pp. 107–122, 06 2011.
- [36] A. Sakurai, A. Hayashi, W. J. Munro, and K. Nemoto, “Simple hamiltonian dynamics as a powerful resource for image classification,” *Phys. Rev. A*, vol. 111, p. 052432, May 2025.
- [37] A. Hayashi, A. Sakurai, S. Nishio, W. J. Munro, and K. Nemoto, “Impact of the form of weighted networks on the quantum extreme reservoir computation,” *Phys. Rev. A*, vol. 108, no. 4, p. 042609, 2023.
- [38] K. Fujii and K. Nakajima, “Harnessing disordered-ensemble quantum dynamics for machine learning,” *Physical Review Applied*, vol. 8, p. 024030, 8 2017.
- [39] G. Angelatos, S. A. Khan, and H. E. Türeci, “Reservoir computing approach to quantum state measurement,” *Phys. Rev. X*, vol. 11, p. 041062, Dec 2021.
- [40] P. Mujal, J. Nokkala, R. Martínez-Peña, G. L. Giorgi, M. C. Soriano, and R. Zambrini, “Analytical evidence of nonlinearity in qubits and continuous-variable quantum reservoir computing,” *Journal of Physics: Complexity*, vol. 2, p. 045008, nov 2021.
- [41] W. Xia, J. Zou, X. Qiu, F. Chen, B. Zhu, C. Li, D.-L. Deng, and X. Li, “Configured quantum reservoir computing for multi-task machine learning,” *Science Bulletin*, vol. 68, pp. 2321–2329, 10 2023.
- [42] A. Sannia, R. Martínez-Peña, M. C. Soriano, G. L. Giorgi, and R. Zambrini, “Dissipation as a resource for quantum reservoir computing,” *Quantum*, vol. 8, p. 1291, 3 2024.
- [43] R. Martínez-Peña, G. L. Giorgi, J. Nokkala, M. C. Soriano, and R. Zambrini, “Dynamical phase transitions in quantum reservoir computing,” *Physical Review Letters*, vol. 127, p. 100502, 9 2021.
- [44] N. Götting, F. Lohof, and C. Gies, “Exploring quantum mechanical advantage for reservoir computing,” *Physical Review A*, vol. 108, 2 2023.
- [45] R. Martínez-Peña, J. Nokkala, G. L. Giorgi, R. Zambrini, and M. C. Soriano, “Information processing capacity of spin-based quantum reservoir computing systems,” *Cognitive Computation*, vol. 15, pp. 1440–1451, 9 2023.
- [46] P. Mujal, “Quantum reservoir computing for speckle disorder potentials,” *Condensed Matter*, vol. 7, p. 17, 1 2022.
- [47] J. Chen and H. I. Nurdin, “Learning nonlinear input–output maps with dissipative quantum systems,” *Quantum Information Processing*, vol. 18, no. 7, p. 198, 2019.
- [48] K. Nakajima, K. Fujii, M. Negoro, K. Mitarai, and M. Kitagawa, “Boosting computational power through spatial multiplexing in quantum reservoir computing,” *Physical Review Applied*, vol. 11, no. 3, p. 034021, 2019.
- [49] Q. H. Tran and K. Nakajima, “Higher-order quantum reservoir computing,” *arXiv preprint arXiv:2006.08999*, 2020.
- [50] R. Martínez-Peña, J. Nokkala, G. L. Giorgi, R. Zambrini, and M. C. Soriano, “Information processing capacity of spin-based quantum reservoir computing systems,” *Cognitive Computation*, pp. 1–12, 2020.
- [51] S. Ghosh, A. Opala, M. Matuszewski, T. Paterek, and T. C. H. Liew, “Quantum reservoir processing,” *npj Quantum Information*, vol. 5, p. 35, 4 2019.
- [52] Q. H. Tran, S. Ghosh, and K. Nakajima, “Quantum-classical hybrid information processing via a single quantum system,” *Physical Review Research*, vol. 5, p. 43127, 2023.
- [53] G. Llodrà, C. Charalambous, G. L. Giorgi, and R. Zambrini, “Benchmarking the role of particle statistics in quantum reservoir computing,” *Advanced Quantum Technologies*, vol. 6, p. 2200100, 1 2023.
- [54] M. Kornjača, H.-Y. Hu, C. Zhao, J. Wurtz, P. Weinberg, M. Hamdan, A. Zhdanov, S. H. Cantu, H. Zhou, R. A. Bravo, K. Bagnall, J. I. Basham, J. Campo, A. Choukri, R. Deangelo, P. Frederick, D. Haines, J. Hammett, N. Hsu, M.-G. Hu, F. Huber, P. N. Jepsen, N. Jia, T. Karolyshyn, M. Kwon, J. Long, J. Lopatin, A. Lukin, T. M. Macrì, O. M. Marković, L. A. Martínez-Martínez, X. Meng, E. Ostroumov, D. Paquette, J. Robinson, P. S. Rodriguez, A. Singh, N. Sinha, H. Thoreen, N. Wan, D. Waxman-Lenz, T. Wong, K.-H. Wu, P. L. S. Lopes, Y. Boger, N. Gemelke, T. Kitagawa, A. Keesling, X. Gao, A. Bylinskii, S. F. Yelin, F. Liu, and S.-T. Wang, “Large-scale quantum reservoir learning with an analog quantum computer,” 7 2024.

- [55] R. A. Bravo, K. Najafi, X. Gao, and S. F. Yelin, “Quantum reservoir computing using arrays of rydberg atoms,” *PRX Quantum*, vol. 3, p. 030325, 8 2022.
- [56] L. Henriët, L. Beguin, A. Signoles, T. Lahaye, A. Browaeys, G.-O. Reymond, and C. Jurczak, “Quantum computing with neutral atoms,” *Quantum*, vol. 4, p. 327, 9 2020.
- [57] F. Perciavalle, F. Plastina, M. Pissarra, and N. L. Gullo, “Predicting fermionic densities using a projected-quantum-kernel method,” *Phys. Rev. A*, vol. 112, no. 2, p. 022620, 2025.
- [58] F. Perciavalle, D. Rossini, J. Polo, O. Morsch, and L. Amico, “Quantum superpositions of current states in rydberg-atom networks,” *Phys. Rev. Res.*, vol. 6, p. 043025, Oct 2024.
- [59] M. Kramer, “Autoassociative neural networks,” *Computers & Chemical Engineering*, vol. 16, no. 4, pp. 313–328, 1992. Neural network applications in chemical engineering.
- [60] G. E. Hinton and R. S. Zemel, “Autoencoders, minimum description length and helmholtz free energy,” in *Neural Information Processing Systems*, 1993.
- [61] D. E. Rumelhart, G. E. Hinton, and R. J. Williams, “Learning representations by back-propagating errors,” *Nature*, vol. 323, pp. 533–536, 1986.
- [62] G. E. Hinton and R. R. Salakhutdinov, “Reducing the dimensionality of data with neural networks,” *Science*, vol. 313, no. 5786, pp. 504–507, 2006.
- [63] Y. Lecun, C. Cortes, and C. J. Burges, “Mnist handwritten digit database.” *ATT Labs [Online]*. Available: <http://yann.lecun.com/exdb/mnist>, 2010.
- [64] H. Xiao, K. Rasul, and R. Vollgraf, “Fashion-MNIST: a novel image dataset for benchmarking machine learning algorithms,” 2017. <https://arxiv.org/abs/1708.07747>.
- [65] A. Krizhevsky, “Learning multiple layers of features from tiny images,” tech. rep., University of Toronto, 2009. <https://www.cs.toronto.edu/~kriz/cifar.html>.
- [66] P. Calabrese and J. Cardy, “Evolution of entanglement entropy in one-dimensional systems,” *Journal of Statistical Mechanics: Theory and Experiment*, vol. 2005, p. P04010, apr 2005.
- [67] J. I. Latorre and A. Riera, “A short review on entanglement in quantum spin systems,” *Journal of Physics A: Mathematical and Theoretical*, vol. 42, p. 504002, dec 2009.